Synthesis, Structure and Reactivity of a Mononuclear *N,N,O*-Bound Fe(II) α-Keto-Acid Complex

Emily C. Monkcom,[a] Laura Gómez,[b] Martin Lutz,[c] Shengfa Ye,[d] Eckhard Bill+,[e] Miquel Costas,[f] and Robertus J. M. Klein Gebbink*[a]

A bulky, tridentate phenolate ligand (**Im^Ph2^NNO^tBu^**) was used to synthesise the first example of a mononuclear, facial, *N,N,O*-bound iron(II) benzoylformate complex, [Fe(Im^Ph2^NNO^tBu^)(BF)] (**2**). The X-ray crystal structure of **2** reveals that the iron centre is pentacoordinate ($\tau = 0.5$), with a vacant site located *cis* to the bidentate BF ligand. The Mössbauer parameters of **2** are consistent with high-spin iron(II), and are very close to those reported for α-ketoglutarate-bound non-heme iron enzyme active sites. According to NMR and UV-vis spectroscopies, the structural integrity of **2** is retained in both coordinating and non-coordinating solvents. Cyclic voltammetry studies show that the iron centre has a very low oxidation potential and is more prone to electrochemical oxidation than the redox-active phenolate ligand. Complex **2** reacts with NO to form a $S = {}^{3}/_{2}$ {FeNO}^{7} adduct in which NO binds directly to the iron centre, according to EPR, UV-vis, IR spectroscopies and DFT analysis. Upon O_2 exposure, **2** undergoes oxidative decarboxylation to form a diiron(III) benzoate complex, [Fe$_2$(Im^Ph2^NNO^tBu^)$_2$(μ$_2$-OBz)(μ$_2$-OH)$_2$]$^+$ (**3**). A small amount of hydroxylated ligand was also observed by ESI-MS, hinting at the formation of a high-valent iron(IV)-oxo intermediate. Initial reactivity studies show that **2** is capable of oxygen atom transfer reactivity with O_2, converting methyl(*p*-tolyl)sulfide to sulfoxide.

[a] Dr. E. C. Monkcom, Prof. Dr. R. J. M. Klein Gebbink
Organic Chemistry and Catalysis
Institute for Sustainable and Circular Chemistry
Utrecht University
Universiteitsweg 99, 3584 CG Utrecht, The Netherlands
E-mail: r.j.m.kleingebbink@uu.nl

[b] Dr. L. Gómez
Serveis Tècnics de Recerca
Universitat de Girona
Pic de Peguera 15, Parc Cientific
17003 Girona, Spain

[c] Dr. M. Lutz
Structural Biochemistry
Bijvoet Centre for Biomolecular Research
Utrecht University
Universiteitsweg 99
3584 CG Utrecht, The Netherlands

[d] Prof. Dr. S. Ye
State Key Laboratory of Catalysis
Dalian Institute of Chemical Physics
Chinese Academy of Sciences
457 Zhongshan Road, Dalian 116023, China

[e] Dr. E. Bill+
Max-Planck-Institut für Chemische Energiekonversion
45470 Mülheim an der Ruhr, Germany

[f] Prof. Dr. M. Costas
Institut de Química Computacional i Catàlisi
Universitat de Girona
Pic de Peguera 15, Parc Cientific
17003 Girona, Spain

[+] Deceased October 6, 2022

Introduction

α-Ketoglutarate (αKG) dependent oxidases and oxygenases are widely distributed across prokaryote, eukaryote and archaea organisms and constitute one of the largest sub-classes of mononuclear non-heme iron enzymes.[1–3] Their protein fold comprises a β-strand "jellyroll" motif, which chelates to a single iron(II) centre by means of two histidine residues (His) and a carboxylate group (Asp/Glu), collectively known as the 2-His-1-Carboxylate facial triad (2H1C).[4,5] More recently, αKG-dependent halogenase enzymes have also been identified, although these enzymes possess a 2-His-1-halogen motif at their active site instead of the typical 2H1C.[6–8] In general, αKG-dependent enzymes combine the oxidative decarboxylation of their αKG co-substrate with the 2-electron oxidation of their substrate, using O_2 as the oxidant.[1–3,5,9,10] Succinate and CO_2 are formed simultaneously as by-products (Scheme 1).
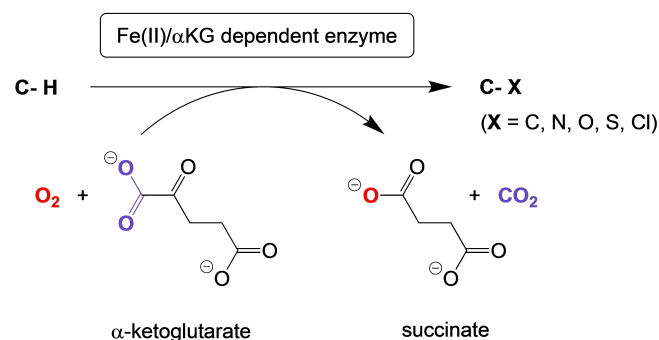
Scheme 1. The oxidative functionalisation of C–H bonds by αKG-dependent non-heme iron enzymes. During this process, αKG is converted to succinate and CO_2.

Chemistry–A European Journal

Research Article
doi.org/10.1002/chem.202302710

Chemistry
Europe
European Chemical
Societies Publishing

Since their initial discovery in the 1960s, these enzymes are now known to catalyse an astoundingly diverse set of reactions, including (di)hydroxylation,[11–14] demethylation (via methyl group hydroxylation),[15–17] epoxidation,[18,19] chlorination,[6,8,20] desaturation,[14,21–25] ring-expansion,[24] cyclization,[13,25] C(sp²)–C-(sp³) coupling,[13,26] epimerization[25,27] and endo-peroxidation.[28,29]

Over the decades, different aspects of the superfamily of αKG-dependent non-heme iron enzymes have been extensively reviewed, including their reaction scope and diversity,[1–3,9,30,31] the biosynthetic pathways towards natural products,[12,15,32,33] enzyme mechanism and spectroscopy,[2,5,10,34–40] as well as mechanistic investigations by means of biomimetic model systems.[3,10,41] The malfunction of αKG-dependent non-heme iron enzymes is closely associated to several human diseases, including anaemia,[42] cancer,[43] Hawkinsinuria,[44,45] Refsum disease,[46] and Ehlers-Danlos syndrome (type IV).[47–49] Gaining a better understanding of the structure and function of these enzymes therefore remains a long-standing biomedical goal for the appropriate treatment of these diseases using, for instance, small molecular therapeutic agents that inhibit or modulate enzyme activity.[49,54–59] Many of the reactions catalysed by αKG-dependent iron enzymes are synthetically challenging and involve highly selective late-stage functionalisation. Those relating to penicillin and cephalosporin biosynthesis have faced particular scrutiny by the medicinal and pharmaceutical communities and have even prompted the commercial application of enzymes as biocatalysts in antibiotic production (e.g. cephalosporin C synthase (CAS) from *A. chrysogenum*).[60] More recently, the application of αKG-dependent enzymes in chemo-enzymatic synthesis has also been explored.[61]
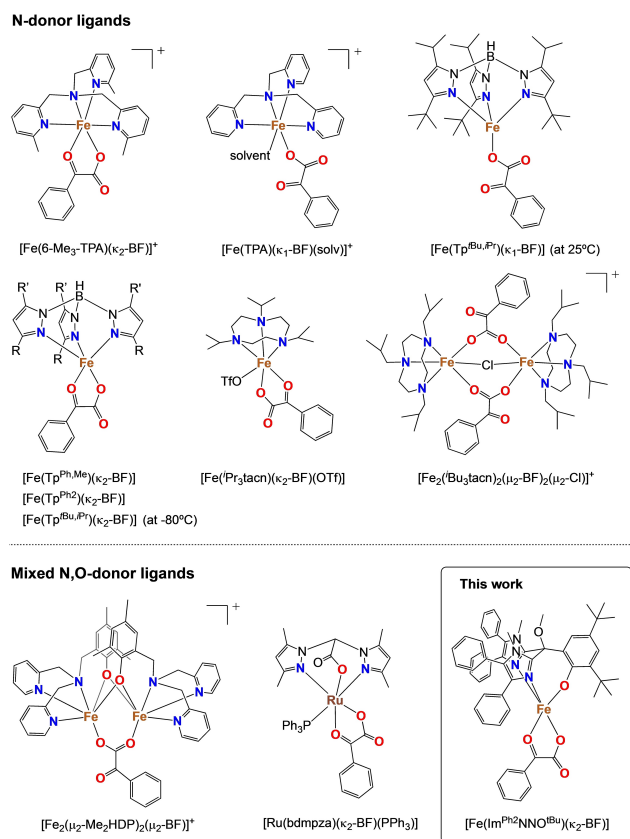
Intense kinetic, spectroscopic and computational investigations have enabled a consensus mechanism to be put forward, depicted in Figure 1A.[3,11,39] Catalysis begins with the bidentate coordination of the αKG co-substrate to the iron centre through its C1 carboxylate and C2 keto groups, displacing two of the three water molecules from the resting state (**A**) and forming a new six-coordinate ferrous complex (**B**).[24,62] Next, the substrate enters the active site cavity and binds in the vicinity of the iron centre, displacing the third water molecule. This generates a five-coordinate ferrous complex (**C**) that is highly reactive to O_2 (Figure 1C).[62–65] Upon O_2 binding, a transient Fe^{III}-superoxide intermediate (**D**) forms, whose distal oxygen atom performs a nucleophilic attack on the αKG C2 carbon atom. This produces a cyclic Fe–O–O–C intermediate (**E**), best described as a Fe^{IV}-peroxy species on the basis of DFT calculations.[66] This intermediate undergoes rapid decarboxy-lation to afford a succinate-bound $Fe^{IV}=O$ intermediate (**F**), which is responsible for substrate H-atom abstraction (HAA).[11,36,38,64,67–68] Following HAA, an Fe^{III}—OH intermediate is formed (**G**),[11] whose hydroxyl group recombines with the substrate radical,[34,69] affording the hydroxylated product and an Fe^{II}-succinate species (**H**).[37] Finally, succinate and the hydroxylated product are released from the active site and water molecules re-populate the vacant sites.

Developing synthetic biomimetic iron complexes is a well-established strategy for studying the reactivity of non-heme iron enzymes and for developing novel iron-based oxidation catalysts. Numerous iron(II)-α-keto-acid complexes have been reported in the past, featuring a polydentate N-donor ligand in combination with an αKG surrogate such as benzoylformate (BF), pyruvate (PRV) or phenylpyruvate (HPP). These are generally termed *functional* model complexes, as they aim to reproduce important mechanistic aspects of enzyme function without necessarily incorporating all structural elements of the enzyme active site, such as the anionic O-donor of the 2H1C. Selected examples of iron(II) benzoylformato functional model complexes are depicted in Figure 2. These complexes demon-
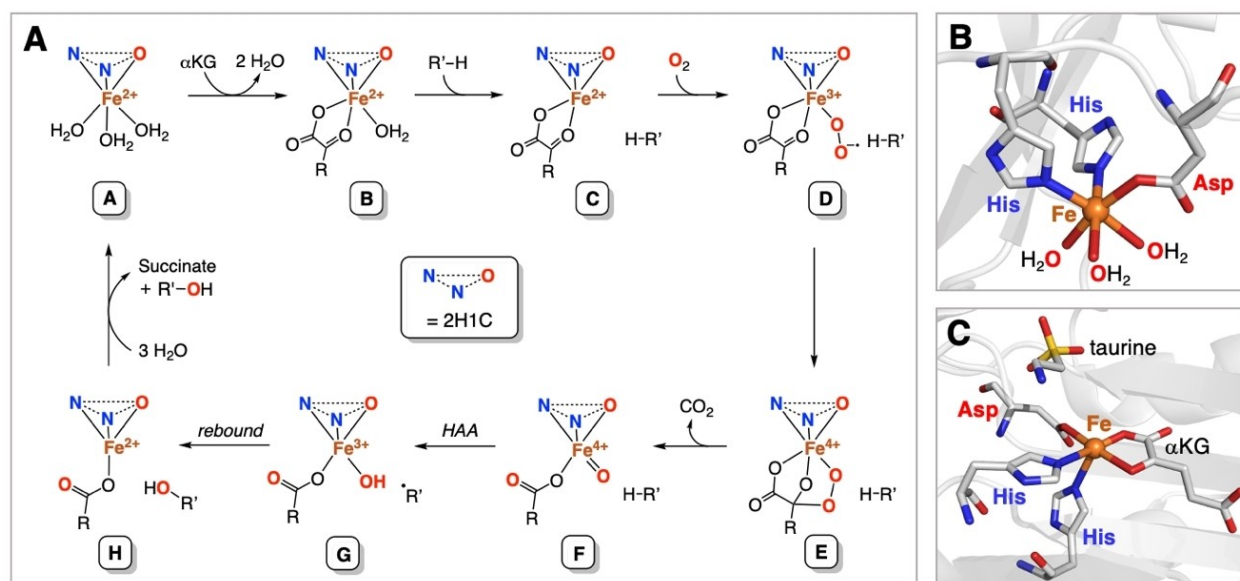
Figure 1. A: Generally accepted mechanism for αKG-dependent non-heme iron hydroxylase enzymes. **B**: Protein crystal structure of the resting state of DAOCS (PDB 1RXF), highlighting the facial coordination of the 2H1C.[24] **C**: Protein crystal structure of the [Fe-TauD-αKG-taurine] enzyme complex for TauD (PDB 1OS7).[70] Carbon, iron, nitrogen, oxygen and sulfur are depicted in grey, orange, blue, red and yellow, respectively.

Chemistry–A European Journal

Research Article
doi.org/10.1002/chem.202302710

Chemistry Europe
European Chemical
Societies Publishing

Figure 2. Selected examples of structurally characterised iron(II) or ruthenium(II) benzoylformate complexes. Top: complexes supported by tripodal N3 and N4 ligands. Bottom: complexes supported by mixed N,O-donor ligands.[±]

strate that a delicate balance exists between their structure and their reactivity, which is significantly affected by the steric bulk of the supporting ligand and the coordination mode of the α-keto-acid. For instance, Que and co-workers have employed the tripodal, tetradentate N4 ligands **TPA** and **6-Me$_3$-TPA** to synthesise cationic, high-spin iron(II)-BF complexes of octahedral geometry.[71–73] In the case of [Fe^{II}(TPA)(κ_1-BF)(solv)]$^+$, the binding pocket at the iron centre is large enough to accommodate solvent coordination, leading to monodentate BF coordination. In contrast, the greater steric bulk of the supporting ligand in [Fe^{II}(6-Me$_3$-TPA)(κ_2-BF)]$^+$ prevents solvent ligation to the iron, ensuring bidentate BF coordination. Both [Fe^{II}(TPA)(κ_1-BF)(solv)]$^+$ and [Fe^{II}(6-Me$_3$-TPA)(κ_2-BF)]$^+$ undergo oxidative decarboxylation in the presence of O$_2$ to afford the corresponding benzoate complexes in quantitative yield.[72] However, these reactions are rather sluggish, taking place over the course of several days. The slowness of these reactions is attributed to the coordinative saturation of the iron centre, which requires ligand dissociation in order for O$_2$ to bind.[73]

Similar studies have been conducted using the tris(pyrazolyl)borate ligand family (**Tp**), which provides a monoanionic, tripodal N3 coordination motif. Valentine and co-workers showed that complex [Fe^{II}(Tp^{Me2})(κ_2-BF)], which features one of the smallest Tp variants, is extremely reactive to air, even in its solid state, and undergoes oxidative decarboxylation to

form the corresponding benzoate complex quantitatively within 2 min.[74] In contrast, Moro-oka and co-workers prepared complex [Fe^{II}(Tp^{3tBu,5iPr})(BF)], whose supporting ligand is so bulky that it is unreactive to O$_2$.[75] In later work, the groups of Que and Paine showed that complexes [Fe^{II}(Tp^{Ph2})(κ_2-BF)],[76,77] [Fe^{II}-(Tp^{Ph,Me})(κ_2-BF)],[78] and [Fe^{II}(Tp^{iPr2})(κ_2-BF)],[79] which feature ligands of "medium" bulk, can undergo quantitative oxidative decarbyoxlation in the presence of O$_2$ and can catalytically oxidise simple substrates such as sulfides and olefins to their corresponding sulfoxides and epoxides, respectively. Recently, Costas and co-workers employed the neutral, tridentate N3 ^{i}Pr$_3$tacn ligand to prepare mononuclear iron complex [Fe^{II}-(^{i}Pr$_3$tacn)(κ_2-BF)(OTf)], which oxidatively decarboxylates in the presence of O$_2$ and catalytically oxidises sulfides to their corresponding sulfoxides.[80] In contrast, the reduced steric bulk of the related ^{i}Bu$_3$tacn ligand was shown to promote the formation of a BF-bridged diiron(II) complex, [Fe$_2$(^{i}Bu$_3$tacn)$_2$(μ_2-BF)$_2$(μ_2-Cl)], that does not show any oxygen atom transfer (OAT) reactivity.

In past studies, it has been emphasised that the facial *N,N,O* coordination of the 2H1C plays an important role in enzyme reactivity by anchoring the iron centre in the protein scaffold and providing three mutually-*cis* coordination sites at which catalysis takes place.[62,81] It has also been suggested that the non-coordinated oxygen atom of the 2H1C carboxylate group partakes in H-bonding with the iron-bound water molecule in intermediate **B**, which could help prevent premature O$_2$ reactivity of the active site by ensuring coordinative saturation.[63,82] Thirdly, the anionic charge of the 2H1C has been proposed to stabilise the coordination of αKG in its mono-anionic α-keto-acid form instead of its tautomeric dianionic enolate form.[82,83] This ensures decarboxylation of the acid through C1—C2 cleavage and allows the co-substrate to provide the two electrons necessary for generation of the high-valent ferryl intermediate. Finally, the anionic O-donor also helps lower the Fe^{II}/Fe^{III} redox potential, which is important for enabling O$_2$ reactivity of the enzyme active site.

Strikingly, studies employing mixed *N,O*-donor ligands for *structurally* modelling the 2H1C at αKG-dependent enzyme active sites are scarce. This is largely due to the fact that very few tridentate *N,N,O* ligands have been reported that support the formation of mononuclear, monoligated iron complexes.[84–87] Typically, problems are encountered through the formation of homoleptic bis-ligand complexes, the formation of polynuclear complexes due to bridging O-donor coordination modes, or disruption of the *N,N,O* triad due to labile N- or O-donors.[88,89] To the best of our knowledge, the dinuclear complex [Fe$_2$(μ_2-Me$_2$HDP)$_2$(μ_2-BF)], reported by the group of Que (Figure 2), is the only structurally characterised iron(II) benzoylformato complex to date that features a mixed *N,O*-donor ligand.[90] Burzlaff and co-workers have since reported a mononuclear Ru(II) complex, [Ru(bdmpza)(κ_2-BF)(PPh$_3$)], which features a bis(pyrazolyl)-acetate ligand (Figure 2).[91] However, the synthesis of mononuclear Fe-BF complexes supported by a facial, κ_3-*N,N,O* ligand remains elusive, which reflects how challenging and under-developed the
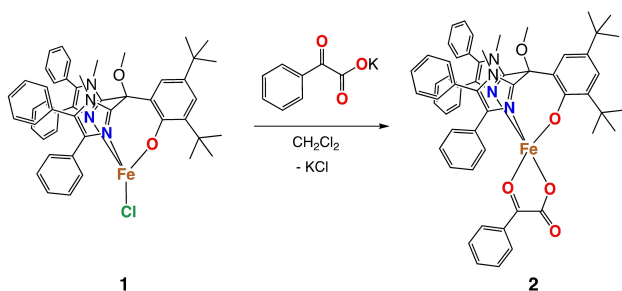
coordination chemistry of these ligands is compared to that of polydentate N-donor ligands.

In this study, we have employed a bulky *N,N,O* phenolate ligand (**Im^Ph2^NNO^tBu^**)[84] to synthesise a mononuclear non-heme iron(II) benzoylformato complex, [Fe(Im^Ph2^NNO^tBu^)(BF)] (Figure 2). We report the solid- and solution-state structure of the complex using X-ray crystal structure determination, UV-vis and NMR spectroscopies, and its electronic structure by means of Mössbauer spectroscopy and SQUID magnetometry. Using cyclic voltammetry, we have also investigated the electrochemical behaviour of the complex in acetonitrile solution and show that the iron centre has a very low oxidation potential. Accordingly, we examined the reactivity of the complex with respect to O_2 and NO, the latter using trityl-S-nitrosothiol (Ph_3CSNO) as a convenient NO donor.

Results and Discussion

Complex Synthesis

Complex [Fe(Im^Ph2^NNO^tBu^)(BF)] (**2**) was synthesised according to the reaction depicted in Scheme 2. [Fe(Im^Ph2^NNO^tBu^)(Cl)] (**1**), whose preparation has previously been reported by our group,[84] was dissolved in CH_2Cl_2 and one equivalent of potassium benzoylformate (K-BF), suspended in CH_2Cl_2, was added dropwise to the solution. The reaction was left to stir overnight, during which time the colour of the mixture changed from pale brown to deep blue. The reaction was filtered and all solvent was removed under vacuum. The crude blue solid was washed with hexane and dried, affording **2** as a bright blue powder in 92% yield. IR analysis of **2** reveals a strong absorption band at 1673 cm^{-1}, assigned to the BF carboxylate stretching vibration (Figure S1). The absence of an O—H absorption band also confirms the anionic nature of both the supporting ligand and the BF co-ligand in **2**. Positive mode ESI-HRMS analysis of **2** in acetonitrile shows a signal at $m/z=$ 941.3326, assigned to the $[2+Na]^+$ ion (calc $m/z=941.3337$). However, the relative intensity of this signal is rather weak compared to the signals observed at $m/z=810.3462$ and $m/z=$ 828.3557, which correspond to ions $[Fe(Im^{Ph2}NNO^{tBu})(MeCN)]^+$ and $[Fe(Im^{Ph2}NNO^{tBu})(MeCN)(H_2O)]^+$, respectively (Figure S3). We attribute the greater relative abundancy of these ions to their natural positive charge, in contrast to the neutral charge of **2**.

X-Ray Crystal Structure Analysis

Dark blue crystals suitable for X-ray diffraction were obtained from slow vapour diffusion of hexane into a THF solution of **2**. The X-ray crystal structure of **2** is depicted in Figure 3, with selected bond lengths and bond angles provided in Table S2. Importantly, this structure demonstrates the clean substitution of the chloride ligand in **1** for the benzoylformate ligand, with retention of the supporting ligand's tripodal *N,N,O* coordination motif. The BF ligand binds to the iron in a bidentate fashion, through asymmetric coordination of its carboxylate (O12) and keto (O32) groups. The pentacoordinate structure of **2** has a geometry that lies exactly between square pyramidal and trigonal bipyramidal, as defined by its geometric index ($\tau =$ 0.5).[92] Assuming a square pyramidal geometry, the equatorial plane comprises the BF acid (O12) and keto (O32) groups as well as the supporting phenolate (O11) and imidazole (N31) donors. The apical position is occupied by the imidazole nitrogen N11. The steric clash between the BF phenyl group and the phenolate *ortho*-^tBu substituent causes the BF ligand to "tilt" towards one of the imidazole groups, which results in a relatively good degree of accessibility at the iron centre.

A putative binding site for small molecules like O_2 in **2** is hypothesised as being *trans* to N11, which would create an octahedron when occupied. The Fe—O_{phen} bond length of 1.9235(13) Å is slightly elongated compared to that reported for **1**, which reflects the increase in coordination number for **2**. The Fe—O_{acid} and Fe—O_{keto} bond lengths of 2.0105(14) Å and 2.1775(13) Å, respectively, reflect the different charges of the oxygen atoms. The α-keto-acid moiety is nearly planar, with a O—C—C—O torsion angle of 3.4(3)°. The Fe—O_{acid} bond length in **2** is slightly longer compared to those reported for pentacoordinate Fe-BF complexes supported by Tp ligands.[75,76,78] We attribute this to the more localised negative charge of the **Im^Ph2^NNO^tBu^** ligand, which quenches the Lewis acidity of the iron centre. The Fe—N bond lengths are characteristic of a high-

Scheme 2. The synthesis of [Fe(Im^Ph2^NNO^tBu^)(BF)] (**2**).
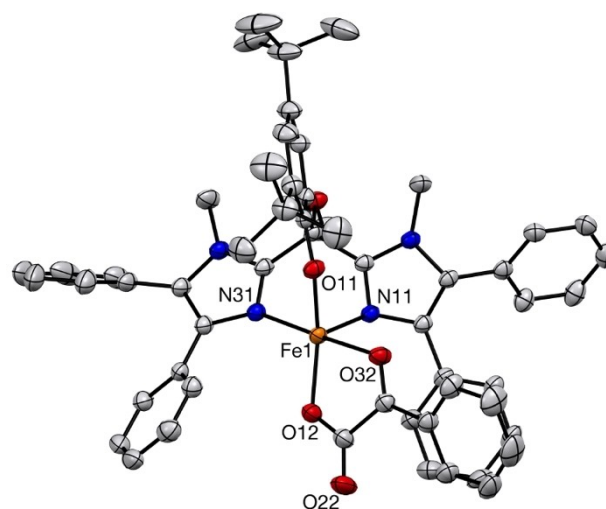
Figure 3. Displacement ellipsoid plot of **2** (50% probability level). All H atoms and co-crystallised solvent molecules have been omitted for clarity.

Chemistry–A European Journal

Research Article
doi.org/10.1002/chem.202302710

Chemistry Europe
European Chemical
Societies Publishing

spin iron(II) centre bound to an imidazole-containing *N,N,O* ligand.[84,85,88,89]

UV-vis Spectroscopy

One of the most distinctive ways to examine the solution-state structure of αKG-dependent iron enzymes and their model complexes is through UV-vis absorption spectroscopy. Bidentate α-keto-acid coordination to iron is well reported to produce distinctive blue-violet coloured complexes.[41] Spectroscopically, this is manifested by a characteristic "trio" of metal-to-ligand charge transfer (MLCT) bands between 500 and 600 nm, that correspond to charge donation from the iron's filled d-orbitals to the low-lying π* orbitals of the planar, conjugated α-keto-acid moiety.[72] Monodentate α-keto-acid coordination modes generally give rise to yellow or orange-coloured solutions that do not exhibit these MLCT bands.[72,80]

Dissolving **2** in either MeCN or CH$_2$Cl$_2$ produces a deep blue solution in both solvents, whose absorption spectra are given in Figure 4. The absorption spectrum of **2** in MeCN features a maximum absorption band at 610 nm (ε = 526 M^{-1} cm^{-1}), shouldered by two other bands at 545 nm and 735 nm. A similar spectrum is obtained in CH$_2$Cl$_2$, with a maximum absorption at 600 nm (ε = 830 M^{-1} cm^{-1}) and two shoulders at 540 and 750 nm.

This demonstrates that the bidentate coordination mode of the BF ligand, which was observed in the X-ray crystal structure of **2**, is retained in solution, in both coordinating and non-coordinating solvents. We note that the optical spectrum of **2** in both MeCN and CH$_2$Cl$_2$ is somewhat red-shifted compared to previously reported Fe-BF complexes, whose maximum absorptions typically range between 531 and 610 nm (see Table S1). We ascribe this to the anionic charge of the phenolate group of the **Im^{Ph2}NNO^{tBu}** ligand, which may help quench the Lewis acidity of the iron(II), thereby decreasing the energy of MLCT bands.

NMR Spectroscopy

Having established the bidentate binding mode of the BF ligand in solution, we were also keen to investigate the temperature-dependent solution state behaviour of **2** by means of NMR spectroscopy. The ^{1}H NMR spectra of **2** recorded in
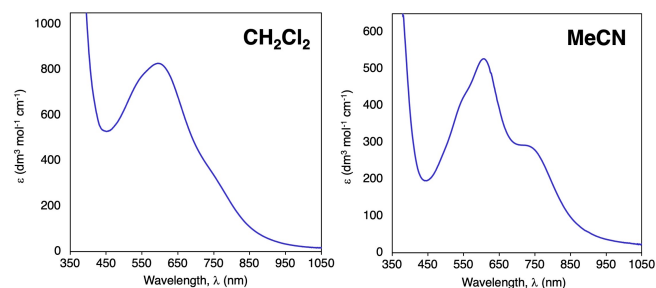
CD$_3$CN and CD$_2$Cl$_2$ contain paramagnetically shifted signals in the range of −5 to 55 ppm (Figure 5).

Using Evans' NMR method, the effective magnetic moment (μ$_{eff}$) of **2** in acetonitrile solution was determined to be 4.45 μ$_B$, which corresponds to a high-spin ($S = 2$) electronic configuration and is consistent with solid-state Mössbauer and SQUID magnetometry data (*vide infra*). Due to their highly broad nature, assignment of the paramagnetic NMR resonances could not be made. However, the number of signals observed for **2** in both solvents is comparable to that previously reported for **1**,[84] whereby it may reasonably be assumed that **2** maintains a monomeric, pentacoordinate structure in solution, akin to that observed in the solid state.

Variable temperature (VT) ^{1}H NMR analysis in both CD$_3$CN and CD$_2$Cl$_2$ shows an increase in magnetisation of **2** as the temperature decreases, consistent with normal Curie behaviour (Figures S4 and S5). Highly linear plots of chemical shift against reciprocal temperature were obtained in CD$_2$Cl$_2$, with intercepts extrapolating to the diamagnetic region at infinite temperature (Figure 5). In CD$_3$CN, slight deviation from linearity of the Curie plot is observed that we ascribe to the more strongly coordinating nature of the solvent, which may induce slight structural rearrangements in solution. Finally, spin crossover phenomena were not observed in either solvent, nor were any significant changes in speciation of the complex detected.
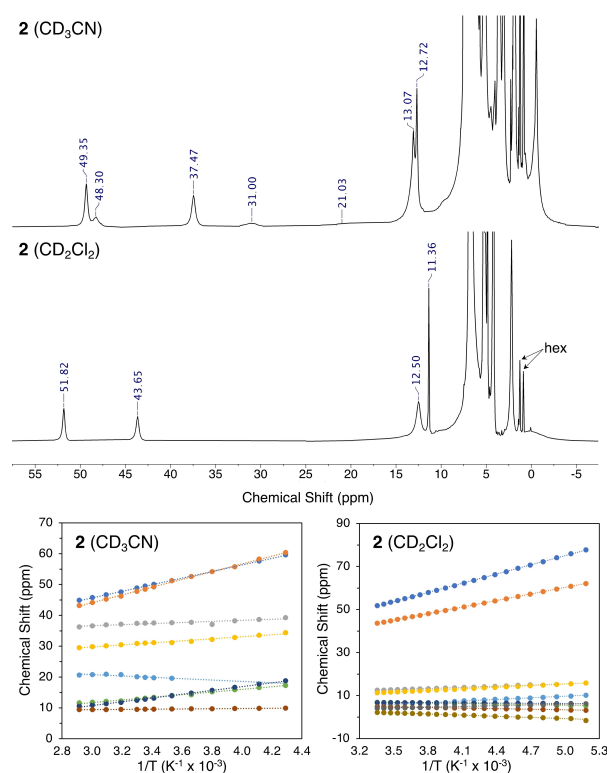
Figure 5. Top: Stacked ^{1}H NMR (400 MHz) spectra of **2** in CD$_3$CN and CD$_2$Cl$_2$, recorded at 25 °C. Spectra are clipped vertically for clarity. Bottom: Curie plots of chemical shift (ppm) versus reciprocal temperature (K^{-1}) for **2** in CD$_3$CN and CD$_2$Cl$_2$.

Figure 4. UV-vis spectra of **2** recorded in CH$_2$Cl$_2$ and MeCN at 25 °C.

Chemistry–A European Journal

Research Article
doi.org/10.1002/chem.202302710

Chemistry
Europe
European Chemical
Societies Publishing

Electronic Structure Analysis

Zero-field ^{57}Fe Mössbauer analysis (80 K, 0 T) of complex **2** produced a single doublet with an isomer shift (δ) value of 1.17 mm s^{-1} and a quadrupole splitting ($|\Delta E_Q|$) of 2.64 mm s^{-1} (Figure 6). These values are typical for a high-spin ($S = 2$) iron(II) system and account for 96% of the total signal abundancy. A small ferric impurity was also detected, accounting for 4% of the total signal abundancy. Compared to **1** ($\delta = 0.94$ mm s^{-1}),[84] the isomer shift of **2** has increased slightly due to the expansion of the coordination sphere from tetracoordinate to pentacoordinate, which causes a slight decrease in metal-ligand bond covalency and therefore a reduction in the s-electron density at the Fe nucleus.[93] The Mössbauer parameters for **2** are very close to those reported for the pentacoordinate αKG-bound active sites of TauD ($\delta = 1.16$ mm s^{-1})[11] and P4H ($\delta = 1.17$ mm s^{-1}).[38]

Slight asymmetry of the quadrupole doublet for **2** is observed, due a slight broadening of the high-energy line. Since integer spin systems cannot be magnetic without an applied field (in contrast to half-integer spin systems), we exclude non-fast paramagnetic relaxation effects as being the cause of this asymmetry. Similarly, we exclude the asymmetry of the spectrum as deriving from any impurities, as the quadrupole double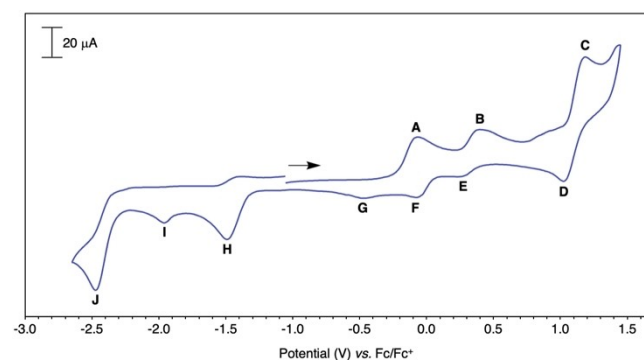t lines integrate equally. Therefore, we attribute the asymmetry to some unresolved (micro)heterogeneity of the iron site. Overall, the Mössbauer parameters obtained for **2** suggest that our structural model is electronically very similar to the pentacoordinate, O$_2$-reactive active sites of αKG-dependent iron enzymes.

Temperature-dependent magnetic susceptibility measurements were conducted by SQUID magnetometry on a powder sample of **2** (Figure 6). The complex has a χT value of 2.8 cm^3 K mol^{-1} at 300 K, consistent with a high-spin iron(II) complex ($S = 2$). Upon cooling, this value remains constant until approx. 50 K, in accordance with normal Curie behaviour. Below 50 K, the χT decreases sharply to approximately 1.1 cm^3 K mol^{-1}, indicative of a sizeable zero-field splitting. No temperature-dependent spin crossover phenomena are observed for **5** in the solid state. Finally, we note that the isotropic g-value of 1.94 is slightly lower than the expected value for a mononuclear high-spin ferrous centre (typically > 2). We attribute this to the small iron(III) impurity present in the sample (likely a Fe^{III}—O—Fe^{III} dimer species with an $S = 0$ ground state), which decreases the overall magnetization of the sample.

Electrochemistry

The redox behaviour of **2** was investigated by cyclic voltammetry (CV) under an inert N$_2$ atmosphere, in acetonitrile solution and using [n-Bu$_4$N]PF$_6$ as a supporting electrolyte. All quoted potentials are referenced versus the ferrocene/ferrocenium couple (Fc/Fc$^+$). The full voltammogram of **2** is displayed in Figure 7. A total of ten different electrochemical responses are observed within the potential range -2.7 to $+1.5$ V (**A**–**J**). Importantly, the section of the voltammogram comprising events **A**–**G** (i.e. between -0.75 V and $+1.50$ V) is very similar, both in terms of waveform and redox potentials, to the cyclic voltammogram previously reported for **1**.[84] We also observe that this region of the voltammogram is (electro)chemically reproducible for several consecutive cycles (Figure S10), as was previously observed for **1**. We therefore hypothesise that these events are related to the structural "unit" formed by the N,N,O ligand and the iron centre, which complexes **1** and **2** have in common. This also provides strong additional evidence that **2**

Figure 6. Top: Zero-field ^{57}Fe Mössbauer spectrum of **2**, recorded at 80 K. Black circles represent the experimental data points. The red trace represents the best combined fit. The green trace corresponds to the best fit for **2** (96% relative abundancy), where $\delta = 1.17$ mm s^{-1} and $|\Delta E_Q| = 2.64$ mm s^{-1}. The blue trace corresponds to an Fe^{3+} impurity (4% relative abundancy), where $\delta = 0.45$ mm s^{-1} and $|\Delta E_Q| = 1.19$ mm s^{-1}. Bottom: Solid-state temperature-dependent magnetic susceptibility of **2**, as measured by SQUID magnetometry. Black circles depict the data points and the red trace depicts the best fit ($g_{x,y,z} = 1.94$, $D = 8.20$ cm^{-1}).


Figure 7. CV of **2** recorded in a 0.1 M [n-Bu$_4$N]PF$_6$ MeCN solution at room temperature, with a scan rate of 100 mV/s.

Chemistry–A European Journal

Research Article
doi.org/10.1002/chem.202302710

Chemistry Europe
European Chemical
Societies Publishing

exists as a single species in MeCN solution, as was previously reported for **1**.[84]

Segmentation experiments enabled the relationship between different electrochemical responses to be established (Figure S13). The first oxidative response, **A**, occurs at -0.07 V and is coupled to a weak reductive response **G** ($E_{p,c} = -0.49$ V). By analogy to **1**, we assign these events to the Fe^{II}/Fe^{III} couple and attribute its irreversible nature to additional structural changes in solution (e.g. solvent coordination) that accompany the formation of the more Lewis-acidic ferric iron, which is known to favour higher coordination numbers. The second oxidation event, **B**, occurs at $+0.40$ V and is ascribed to phenolate oxidation. Oxidation **B** is partnered to two reduction events, **E** and **F**, which supports the hypothesis that multiple species are present in solution. Finally, the electrochemical events **C** and **D** form a quasi-reversible redox couple ($E_{1/2} = 1.12$ V) that we tentatively assign to a Fe^{III}/Fe^{IV} couple. Scanning below -1.0 V, we observe three irreversible reductive responses (**H**–**J**). Interestingly, these electrochemical events cause significant disturbance to the region of the CV containing events **A**–**G**, including severe broadening of the waves, the appearance of new poorly defined features and depletion of the current output (Figure S9). As responses **H**–**J** were not present in the CV previously reported for **1**,[84] we assign these to the BF ligand and propose that its electrochemical reduction prompts the irreversible structural disintegration of **2** in solution.

Our CV assignments are further substantiated by the computational analysis of **2** (Figure 8). Density functional theory (DFT) calculations show the lowest unoccupied molecular orbital (LUMO) to be significantly delocalised across the BF ligand, the iron centre, and the ligand backbone. However, the principal contribution to the LUMO derives from the π^* orbital of the keto group. The highest occupied molecular orbital (HOMO) is calculated as being a singly occupied iron-based d-orbital, supporting the assignment of event A to the Fe^{II}/Fe^{III} redox couple. Finally, we note that the electrochemical oxidation potential of the iron centre in **2** is very low considering the tridentate, anionic nature of the supporting ligand,[84,94] and is a strong indication that **2** reacts readily with O$_2$.
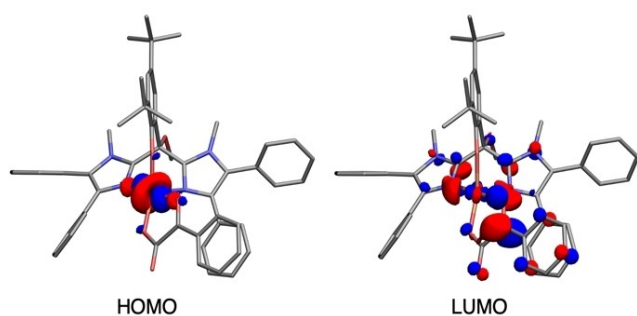
Reactivity to O$_2$

Bubbling O$_2$ (or air) through a solution of **2** in acetonitrile at ambient temperature induces a rapid colour change from blue to violet. The oxidation of **2** by O$_2$ was monitored by absorption spectroscopy, with a spectrum recorded every 6 seconds from the moment at which the contents of the cuvette were exposed to O$_2$ (Figure 9). During the reaction, the MLCT bands of **2** at 745 nm, 606 nm and 540 nm disappear and a new intense band at 525 nm appears with a high extinction coefficient of 3750 M^{-1} cm^{-1}, which we assign to a phenolate-to-iron(III) charge transfer. The intensity of the band at 525 nm overrides the features associated to the coordination of BF and reaches a maximum after 400 seconds, persisting for approx. 1 h before slowly decreasing in intensity. Overnight, the solution changed colour from violet to brown, and finally to yellow over the course of several days. In ^{1}H NMR spectroscopy, exposing an acetonitrile-d_3 solution of **2** to air causes a rapid loss of all paramagnetic signals associated to **2**, presumably due to the formation of an NMR-silent iron species. Some signals in the diamagnetic region are observed, likely corresponding to the free ligand, which could indicate (partial) complex decomposition of the complex in solution upon oxidation.

To gain further insight into the reaction of **2** with O$_2$ in acetonitrile, we resorted to ESI-HRMS analysis. After initial exposure of **2** to O$_2$ (i.e. within less than 5 min), a new positively charged ion was detected with $m/z = 1693.6785$ (Figure S14). This corresponds to a dinuclear ion of the composition [Fe$_2$(L)$_2$(OBz) + 2O + 2H]$^+$ (**3a**), comprising two Fe^{3+} ions, two ligand molecules (L=Im^{Ph2}NNO^{tBu}) and one benzoate molecule (Scheme 3). Two exogenous oxygen atoms and two protons are also incorporated within the structure of **3a**, presumably as two hydroxo ligands, accounting for the single positive charge of this ion. Exposing **2** to isotopically labelled dioxygen (^{18}O$_2$) produces a new ion, **3b**, with $m/z = 1695.6779$ (Figure S20). This corresponds to the incorporation of a single ^{18}O-atom within the ion structure.

Treating a solution of **3a** with labelled water (H$_2$^{18}O) generates ion **3c**, with $m/z = 1697.6836$ (Figure S21). This
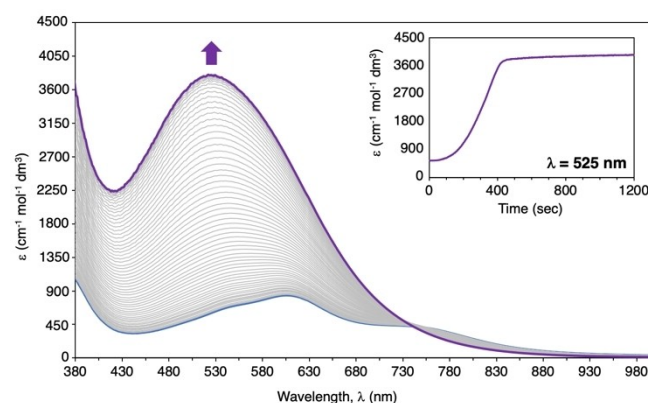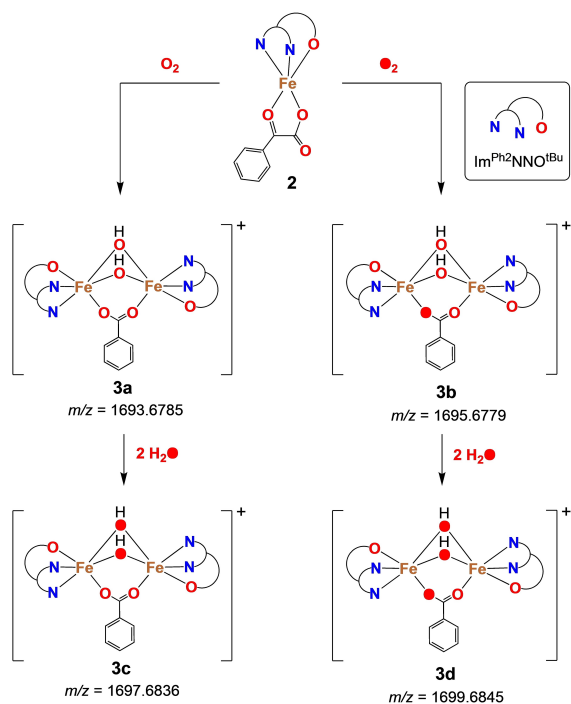

Figure 8. The DFT-calculated HOMO (left) and LUMO (right) obtained for **2**. Isosurfaces are drawn at the ± 0.05 level, with opposite phases drawn in red and blue. H-atoms have been omitted for clarity.

Figure 9. Spectral changes upon exposure of a 0.45 mM solution of **2** in acetonitrile to gaseous O$_2$ at 25 °C. Spectra have been plotted with time intervals of 6 seconds. Insert plot: evolution of the band at 525 nm for the first 20 minutes, in seconds.

Chem. Eur. J. **2024**, *30*, e202302710 (7 of 13)

© 2023 The Authors. Chemistry - A European Journal published by Wiley-VCH GmbH

Chemistry–A European Journal

Research Article
doi.org/10.1002/chem.202302710

Chemistry Europe
European Chemical
Societies Publishing

Scheme 3. The aerobic oxidation of **2** to form **3a-3d**, which feature bis(μ_2-hydroxo)-μ_2-benzoate diiron(III) cores. Structures are proposed on the basis of ESI-MS experiments. ^{18}O-atoms are indicated by filled letters.

accounts for the incorporation of two ^{18}O-atoms within the structure. Similarly, treating a solution of **3b** with excess $H_2^{18}O$ produces a new ion, **3d**, with $m/z = 1699.6845$ (Figure S22), containing three ^{18}O-atoms. On the basis of these observations, we propose that the reaction of **2** with O_2 leads to the oxidative decarboxylation of the BF ligand, whereby one O_2 oxygen atom is incorporated into the benzoate moiety of **3a**. We exclude the incorporation of O_2 into the OH ligands, as we would otherwise have detected an ion with three labelled oxygen atoms after exposing **2** to $^{18}O_2$. Therefore, we propose that the OH ligands derive from traces of water present in the measurement conditions. Interestingly, the use of water was found to enhance the detection of both **3a** and **3b** in ESI-MS, by increasing the relative intensity of the signals. This suggests that the exogenous hydroxo ligands coordinate in a μ_2-bridging fashion and that excess water promotes the formation (and therefore abundance in MS) of these dinuclear ions in solution.

The structural assignment of **3a** is supported by literature precedent, including dinuclear complex $[Fe_2(HDP)_2(\mu_2\text{-}O)(\mu_2\text{-}OBz)]^+$, reported by Que and co-workers, that exhibits a strong phenolate-to-iron(III) charge transfer band at 522 nm ($\varepsilon = 3300\ M^{-1}\,cm^{-1}$).[95] The same group also observed the development of a strong phenolate-to-iron(III) charge transfer band at 562 nm ($\varepsilon = 4300\ M^{-1}\,cm^{-1}$) upon exposing dinuclear complex $[Fe_2(\mu_2\text{-}Me_2HDP)_2(\mu_2\text{-}BF)]^+$ to O_2, which was ascribed to the formation of a μ_2-oxo-μ_2-benzoate diiron(III) core.[90] Coordination modes similar to that proposed for **3a** have previously been reported for tri-bridged μ_2-hydroxo-bis(μ_2-acetate) diiron(III) complexes bearing tris(imidazolyl)phosphine (TIP) and

tris(pyrazolyl)-borate (Tp) ligands,[96,97] as well as di-bridged μ_2-oxo-μ_2-benzoate diiron(III) complexes bearing TPA ligands.[98,99]

Monitoring the reaction of **2** with O_2 over time with ESI-MS showed that the predominant species detected within the first 5 min is **3a**. However, after 20 minutes, another signal at $m/z = 1483.7081$ was detected, corresponding to a bisligated iron(III) species, $[Fe(Im^{Ph2}NNO^{tBu})_2]^+$ (**4**). Both **3a** and **4** were seen to persist for several hours, although the ESI-MS spectrum of the oxidised solution was observed to grow increasingly more complex over time, with new ions forming that we were unable to assign (Figure S15-S17).

The presence of a single benzoate ligand in **3a** does not correspond to the 1:1:1 ligand-metal-benzoate stoichiometry expected for the quantitative oxidative decarboxylation of **2**. Formation of **3a** could therefore be due to the initial formation of an oxoiron(IV) species upon oxidative decarboxylation of **2**, which subsequently comproportionates with the remaining ferrous **2** in solution. Indeed, negative-mode ESI-MS analysis of the organic residue recovered after acidic work-up of the oxidised solution of **2** shows a weak signal at $m/z = 148.7$ assigned to the benzoylformate anion, which provides further evidence that **2** does not undergo quantitative decarboxylation (Figure S19).

Positive mode ESI-MS of the organic residue shows the predominant species to be the ligand (L=Im^{Ph2}NNO^{tBu}), with a strong signal for $[L+H]^+$ observed at $m/z = 715.4$ (calc. $m/z = 715.40$) (Figure 10). In addition, three other weak signals were observed at $m/z = 731.4$, 701.4 and 683.4, which we ascribe, respectively, to products of ligand degradation, namely those of: i) ligand hydroxylation, $[L+OH]^+$ (calc. $m/z = 731.40$), ii) methyl cleavage, $[L-CH_3+2H]^+$ (calc. $m/z = 701.39$), and iii) phenolate oxidation accompanied by methoxy cleavage, $[L-OCH_3]^+$ (calc. $m/z = 683.39$). These last two species indicate that the ligand is somewhat susceptible to oxidative degradation. The product of ligand hydroxylation is a very interesting observation as it provides (indirect) evidence for the formation of a short-lived high-valent iron(IV)-oxo intermediate. Previ-
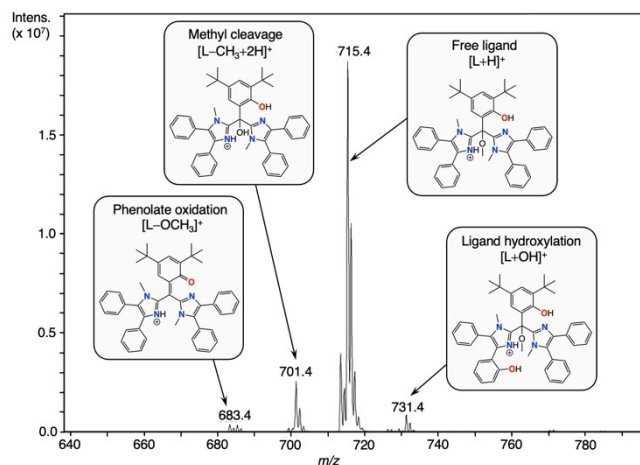
Figure 10. Positive mode ESI-MS spectrum obtained for the organic residue recovered after acidic work-up of an oxidised solution of **2** (shown between m/z 640 and 790). Structures are proposed on the basis of ESI-MS.
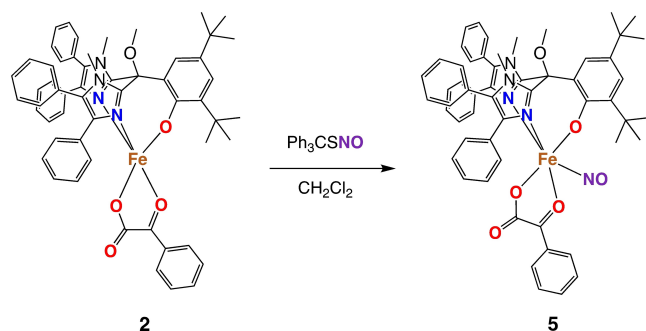
Chemistry–A European Journal

Research Article
doi.org/10.1002/chem.202302710

Chemistry
Europe
European Chemical
Societies Publishing

ously, Que and co-workers also observed intramolecular ligand hydroxylation upon exposure of [Fe(Tp^{Ph2})(μ_2-BF)] and [Fe-(Tp^{iPr2})(μ_2-BF)] to O_2.[76,79] This was proposed to occur due to close proximity of the supporting ligand scaffold and the high-valent Fe^{IV}=O intermediate generated upon oxidative decarboxylation of the BF co-ligand.

Reactivity to NO (using Ph$_3$CSNO)

To further elucidate the changes occurring at the iron centre upon oxidation of **2**, we investigated the *in situ* reaction of **2** with nitric oxide (NO) using trityl-*S*-nitrosothiol (Ph$_3$CSNO) as a convenient NO donor. Use of Ph$_3$CSNO in this manner has been reported to yield iron nitrosyl compounds analogous to those obtained through reaction with NO gas, notably by the groups of Lippard, Meyer, Lehnert and Majumdar.[100–102]

Complex **2** was dissolved in CH$_2$Cl$_2$ at −70 °C and stirred vigorously while a bright green solution of Ph$_3$CSNO in CH$_2$Cl$_2$ was added dropwise to the mixture. Upon complete addition of the nitrosothiol, the mixture was sealed, placed in a dark container and stirred for a period of 90 min while warming to room temperature. During this time, the colour of the solution changed to brown, a colour typically observed for iron nitrosyl complexes. Small aliquots of the reaction mixture were subsequently taken for UV-vis, IR and EPR analysis. Unfortunately, despite numerous attempts, no crystals could be obtained of the proposed nitrosylated product (complex **5** in Scheme 4).

The UV-vis absorption spectrum of the reaction mixture exhibits a new band at 495 nm with a broad shoulder at 640 nm, as well as a feature at 350 nm that shoulders the intense π–π* transition region of the spectrum (Figure 11). Que and co-workers observed similar absorption bands (ascribed to NO-to-Fe charge transfer) for complexes [Fe(6TLA)(κ_1-BF)(NO)](-ClO$_4$) and [Fe(TPA)(κ_1-BF)(NO)](ClO$_4$), although it should be noted that these complexes contain a monodentate BF ligand.[103] In IR spectroscopy, a new peak at 1760 cm^{-1} is observed, which is downshifted compared to free NO (ν_{NO} = 1875 cm^{-1})[104] and distinct from the nitrosothiol precursor (ν_{NO} = 1513 cm^{-1}) (Figure 11).[100] The IR stretch associated to the BF ligand (1673 cm^{-1}) is almost identical compared to that observed for **2**, which shows that the coordination of the BF ligand remains unchanged after reaction with Ph$_3$CSNO.

The X-band EPR spectrum of the reaction mixture, recorded at 100 K, exhibits three features, centred at g = 4.26, 4.00 and 2.02 together with a weak positive peak at g = 9.2 (Figure 11). This EPR data revealed that the sample contains three different paramagnetic species, plotted in sub-spectra **A** (green), **B** (blue) and **C** (grey). **A** corresponds to an $S = ^3/_2$ iron nitrosyl complex, denoted by {FeNO}^{7} according to the Enemark-Feltham notation,[105] and accounts for 78 % of the total paramagnetic species in the sample. This type of NO-adduct is best rationalised as comprising a high-spin ($S = ^5/_2$) Fe^{3+} centre antiferromagnetically coupled to NO$^-$ (S = 1).[106–108] This species exhibits a derivative signal at g_{eff} ~4 and a negative peak at g_{eff} ~2, which can be ascribed to the lower Kramers doublet of the quartet ground spin state according to the $S = ^3/_2$ rhombogram.

Scheme 4. The reaction of **2** with trityl-*S*-nitrosothiol. The structure of **5** is proposed.
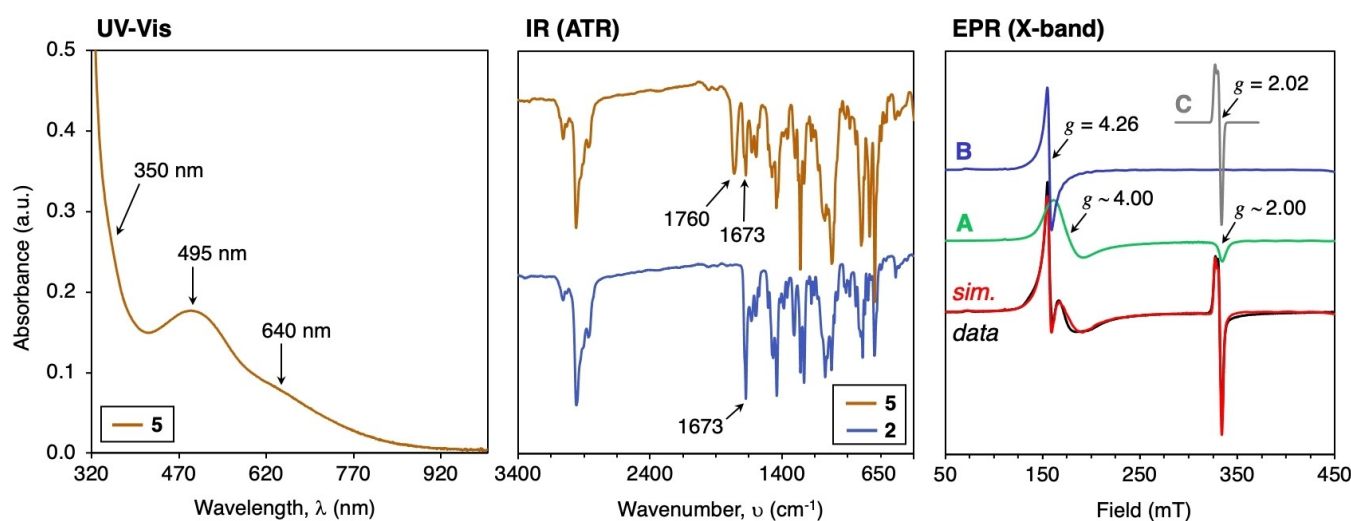
Figure 11. Left: The UV-vis absorption spectrum for **5**, recorded at 25 °C in CH$_2$Cl$_2$. Middle: The stacked IR (ATR) spectra of **2** (blue trace) and **5** (brown trace). Right: X-band EPR spectrum of **5** (black trace) recorded in a CH$_2$Cl$_2$/toluene glass (1 : 1 vol/vol) at 100 K. The simulation is depicted in red, with sub-spectra **A** (green), **B** (blue) and **C** (grey) depicted above. Instrument: frequency = 9.39862 GHz, power = 2.000 mW, modulation amplitude = 1.00 G.

Chemistry–A European Journal

Research Article
doi.org/10.1002/chem.202302710

Chemistry Europe
European Chemical
Societies Publishing

Simulations were performed using the spin Hamilton shown in Equation 1, where D and E are the axial and rhombic zero-field splitting (ZFS) parameters, respectively.

$$H = \beta \cdot S \cdot g \cdot B + D\,[S_z^2 - S\,(S+1)/3] + E\,(S_x^2 - S_y^2) \qquad (1)$$

The best fit was obtained with the following parameters: $D = 5\ \mathrm{cm^{-1}}$ (arbitrarily set), $E/D = 0.046$ (near-axial symmetry), $g_{x,y} = 2.01$ and $g_z = 2.02$. In addition, E/D strain was applied ($\sigma(E/D) = 0.04$) to account for the broadened shape of the spectrum. Such E/D strain usually arises from micro-heterogeneity of the ligand field, typically caused by a (micro)distribution of the molecular structure as caused by solvation effects, etc. Overall, these parameters are in line with those previously reported in the literature for $\{FeNO\}^7$ adducts of αKG-dependent enzymes[108] and relevant model complexes.[103,109,110] On this basis, we assign this species to nitrosylated complex **5** (Scheme 4).

Species **B** is a high-spin ($S = \tfrac{5}{2}$) ferric species, which accounts for 20% of the total paramagnetic species in the sample. Due to its high rhombicity ($E/D = 0.28$), the middle Kramers doublet has three nearly identical g-values that produce an isotropic signal at $g_{\mathrm{eff}} = 4.26$, and its upper or lower Kramer doublet gives a positive peak at $g_{\mathrm{eff}} \sim 9.2$. We speculate that this ferric impurity may form through the 1-electron oxidation of **2** by the Ph$_3$S$^{\cdot}$ radical generated upon homolytic cleavage of Ph$_3$CSNO, this process is likely facilitated by the low oxidation potential of **2**. Species **C** is presumably a $S = \tfrac{1}{2}$ dinitrosyl iron complex (DNIC), as its nearly isotropic signal at $g = 2.01, 2.02, 2.05$ is similar to those found for a large majority of DNICs with an isotropic g-value of 2.03.[109] This minor DNIC impurity accounts for 2% of the total paramagnetic species in the sample.

Using DFT calculations, we examined the electronic structure of two different possible structural isomers of **5**, since the geometric index for **2** ($\tau = 0.5$) suggests that NO could bind at two possible coordination sites (Figure 12). In the first structure (**A**), the NO ligand is coordinated *trans* to an imidazole donor, in the putative vacant site apparent in the solid-state structure of **2**. In the second structure (**B**), the NO ligand is coordinated *trans* to the phenolic oxygen atom. Geometry optimisations of both **A** and **B** produced structures where the nitrosyl ligand adopts a bent configuration and where the spin density is spatially polarised, with the α subset localised on iron and the α subset localised on the NO, consistent with diradical ($S = 1$) NO$^-$ character. **A** was calculated as being approximately 5 kcal mol^{-1} lower in energy than **B**. On this basis, we propose that **A** is the most likely structure for **5**.

In summary, we propose that we have successfully performed the *in-situ* nitroxylation of **2** to form a new $\{FeNO\}^7$ complex, $[\mathrm{Fe(Im^{Ph2}NNO^{tBu})(BF)(NO)}]$ (**5**). However, EPR also suggests that some other (minor) products also form during the reaction. Given the five-coordinate nature of **2**, we envision that NO can bind to the iron's remaining vacant site, *trans* to an imidazole group, without any change in coordination mode needing to occur for either the supporting *N,N,O* ligand or the BF ligand. The fact that **2** can accommodate NO binding means
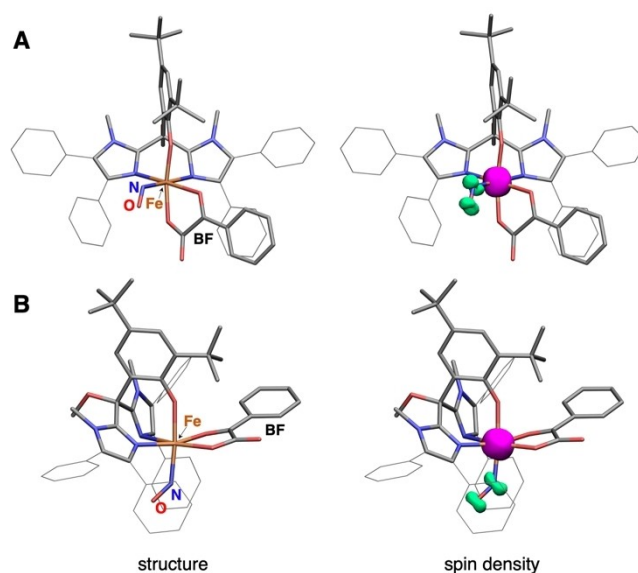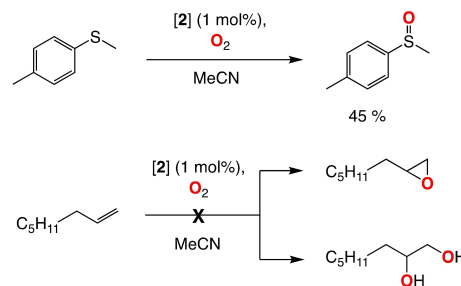

Figure 12. The DFT-optimised gas-phase geometries of the two structural isomers, A and B, for $S = \tfrac{3}{2}$ $\{FeNO\}^7$ adduct **5**. Imidazole phenyl substituents are drawn in the wireframe format for clarity. Spin density isosurfaces for the α (magenta) and β (green) subsets are drawn at the 0.05 level.

O$_2$ is also likely to bind directly to the iron centre, forming a short-lived iron(III) superoxide intermediate whose distal oxygen atom could perform a nucleophilic attack on the BF ligand, leading to the oxidative decarboxylation of **2** in a manner that is mechanistically relevant to αKG-dependent enzymes.

Oxygen Atom Transfer Reactivity

Next, we were keen to investigate **2** as potential oxidation catalyst. The reactivity of **2** was tested by means of interception experiments, using methyl(p-tolyl)sulfide and 1-octene as simple model substrates, and O$_2$ gas as the oxidant (Scheme 5). Overall, **2** was observed to oxidise methyl(p-tolyl)sulfide in 45% yield (with respect to the complex) after 10 min. No further increase in the yield was observed after allowing the reaction to progress for a longer period of time. We speculate that reactivity of **2** is hampered by a process of comproportionation similar to that described for the formation of **3**, whereby ca. 0.5 equiv. of initial complex successfully completes 1 reaction

Scheme 5. Interception experiments using methyl(p-tolyl)sulfide and 1-octene as simple substrates.

Chemistry–A European Journal

Research Article
doi.org/10.1002/chem.202302710

Chemistry
Europe
European Chemical
Societies Publishing

cycle to form a new Fe(II) species that is more easily oxidised than the substrate. For the reaction of **2** with 1-octene, no epoxide or diol products were observed. We therefore conclude that **2** is not active in the oxidation of 1-octene.

Finally, we attempted the oxidation of methyl(*p*-tolyl)sulfide by **2** under catalytic conditions, in the presence of excess benzoylformic acid (H-BF) as a consumable co-substrate. However, no catalytic activity and no product formation was observed. Interestingly, the addition of excess H-BF to a solution of **2** was seen to provoke a swift colour change from blue to purple. This could indicate a change in the structure or speciation of **2** in solution, possibly with involvement of μ_2-bridging BF ligands. Indeed, examples of catalytically inactive BF-bridged diiron(II) complexes have been reported by the groups of Costas[80] and Que.[90] Alternatively, H-BF may disrupt the structure of **2** by protonating its imidazole or phenolate groups. Further investigations are required to elucidate the nature of these transformations and establish the optimal conditions with which catalysis with **2** could successfully occur.

Conclusions

We employed a bulky *N,N,O* phenolate ligand (**Im^{Ph2}NNO^{tBu}**) to synthesise a pentacoordinate, mononuclear non-heme iron(II) benzoylformato complex, [Fe(Im^{Ph2}NNO^{tBu})(BF)] (**2**). Using UV-vis and NMR spectroscopies, we demonstrate that the bidentate BF coordination and the facial *N,N,O* ligand coordination are retained in both coordinating and non-coordinating solvents, across a wide temperature range. The X-ray crystal structure of the complex suggests that a putative vacant site is available for O_2 binding, *cis* to the BF ligand and *trans* to one of the imidazole donors. This qualifies **2** as one of the most faithful structural and electronic models of αKG-dependent iron enzyme active sites to date, and the first model to include an anionic and facial *N,N,O* donor set. This is also reflected by its ^{57}Fe Mössbauer parameters, which are very close to those reported for taurine dioxygenase and proline 4-hydroxylase. Reacting **2** with NO (using Ph$_3$CSNO) affords a $S = {}^3/_2$ {FeNO}^{7} adduct, [Fe(Im^{Ph2}NNO^{tBu})(BF)(NO)] (**5**), whose spectroscopy suggests that NO can bind to the iron centre without disrupting the *N,N,O* coordination of the supporting ligand and the bidentate BF coordination.

Cyclic voltammetry studies show that the iron centre in **2** has a low oxidation potential. Indeed, **2** reacts readily with O_2, generating a metastable purple intermediate. Using UV-vis and ESI-MS measurements, we assign this species as a diiron(III) μ_2-benzoate complex, [Fe$_2$(Im^{Ph2}NNO^{tBu})$_2$(μ_2-OBz)(μ_2-OH)$_2$]$^+$ (**3**). Isotopic labelling experiments using $^{18}O_2$ demonstrate the inclusion of one ^{18}O atom in **3**, most likely within the benzoate moiety. This provides strong evidence that **2** undergoes oxidative decarboxylation in a manner that is mechanistically relevant to the αKG-dependent enzymes. We also observe a small amount of hydroxylated ligand by ESI-MS, which hints at the formation of a high-valent iron(IV)-oxo intermediate. Preliminary reactivity studies show that **2** is capable of oxygen atom transfer (OAT) reactivity and can oxidise methyl(*p*-

tolyl)sulfide to its corresponding sulfoxide in 45 % yield. Current investigations in our laboratory aim to further establish the biomimetic potential of the **Im^{Ph2}NNO^{tBu}** ligand and its iron α-keto-acid complexes, and to provide further insight in the reactivity of complex **2**.

Experimental

All experimental details can be found in the supporting information to this article. CCDC 2133029 contains the supplementary crystallographic data for this paper. The data can be obtained free of charge from The Cambridge Crystallographic Data Centre using the following link: www.ccdc.cam.ac.uk/structures.

Notes

$^+$**TPA** = tri(2-pyridylmethyl)amine; **6TLA** = tris[(6-methyl-2-pyridyl)methyl]amine; **Tp^{3R,5R}** = tris(3,5-disubstituted-pyrazolyl)-borate; **R$_3$tacn** = 1,4,7-tris(alkyl)-1,4,7-triazacyclononane; **bdmpza** = 2,2-bis(3,5-dimethyl-1*H*-pyrazol-1-yl)acetate; **Me$_2$HDP** = 2-((bis(pyridin-2-yl-methyl)amino)methyl)-4,6-dimethylphenol.

Author Contributions

E.C.M and B.K.G. devised the project, designed experiments and wrote the manuscript. E.C.M. performed experiments and analysed the data. L.G. performed HR-ESIMS measurements. M.L. performed X-ray analysis. S.Y. and E.B. provided the Mössbauer, SQUID and EPR data analysis. M.C. contributed to useful scientific discussions and hosted a secondment for E.C.M. All authors provided comments on the manuscript during its preparation.

Acknowledgements

Chemistry–A European Journal

Research Article
doi.org/10.1002/chem.202302710

**Chemistry
Europe**
European Chemical
Societies Publishing

Conflict of Interests

There are no conflicts to declare.

Data Availability Statement

The data that support the findings of this study are available in the supplementary material of this article.

[1] S.-S. Gao, N. Naowarojna, R. Cheng, X. Liu, P. Liu, *Nat. Prod. Rev.* **2008**, *35 (8)*, 792–837.

[2] R. P. Hausinger, *Crit. Rev. Biochem. Mol. Biol.* **2004**, *39 (1)*, 21–68.

[3] C. J. Schofield, R. P. Hausinger, *2-Oxoglutarate-Dependent Oxygenases*, RSC Publishing, Cambridge, **2015**.

[4] L. Que Jr., *Nat. Struct. Biol.* **2000**, *7 (3)*, 182–184.

[5] P. C. A. Bruijnincx, G. van Koten, R. J. M. Klein Gebbink, *Chem. Soc. Rev.* **2008**, *37 (12)*, 2716–2744.

[6] L. C. Blasiak, F. H. Vaillancourt, C. T. Walsh, C. L. Drennan, *Nature* **2006**, *440 (7082)*, 368–371.

[7] A. Timmins, S. P. de Visser, *Catalysts* **2018**, *8*, 314.

[8] A. J. Mitchell, Q. Zhu, A. O. Maggiolo, N. R. Ananth, M. L. Hillwig, X. Liu, A. K. Boal, *Nat. Chem. Biol.* **2016**, *12 (8)*, 636–640.

[9] J. M. Simmons, T. A. Müller, R. P. Hausinger, *Dalton Trans.* **2008**, *38*, 5132–5142.

[10] M. Costas, M. P. Mehn, M. P. Jensen, L. Que Jr., *Chem. Rev.* **2004**, *104 (2)*, 939–986.

[11] J. C. Price, E. W. Barr, B. Tirupati, M. J. Bollinger Jr., C. Krebs, *Biochemistry* **2003**, *42 (24)*, 7497–7508.

[12] K. L. Gorres, R. T. Raines, *Crit. Rev. Biochem. Mol. Biol.* **2010**, *45 (2)*, 106–124.

[13] W. Chen, T. Huang, X. He, Q. Meng, D. You, L. Bai, J. Li, M. Wu, R. Li, Z. Xie, H. Zhou, X. Zhou, H. Tan, Z. Deng, *J. Biol. Chem.* **2009**, *284 (16)*, 10627–10638.

[14] W. Chang, P. Liu, Y. Guo, *Comments Inorg. Chem.* **2018**, *38*, 127–165.

[15] B. I. Fedeles, V. Singh, J. C. Delaney, D. Li, J. M. Essigmann, *J. Biol. Chem.* **2015**, *290 (34)*, 20734–20742.

[16] R. J. Klose, E. M. Kallin, Y. Zhang, *Nat. Rev. Genet.* **2006**, *7 (9)*, 715–727.

[17] C. Yi, C.-G. Yang, C. He, *Acc. Chem. Res.* **2009**, *42 (4)*, 519–529.

[18] J. Lo, H.-J. Liao, Y. Tang, J.-L. Huang, L. Cha, T.-S. Lin, J. L. Lee, I. V. Kurnikov, M. G. Kurnikova, W. Chang, N.-L. Chan, Y. Guo, *J. Am. Chem. Soc.* **2020**, *142 (13)*, 6268–6284.

[19] A. Bräuer, P. Beck, L. Hintermann, M. Groll, *Angew. Chem. Int. Ed.* **2016**, *131 (13)*, 4872–4879.

[20] C. Wong, D. G. Fujimori, C. T. Walsh, C. L. Drennan, *J. Am. Chem. Soc.* **2009**, *131 (13)*, 4872–4879.

[21] N. J. Kershaw, M. E. C. Caines, M. C. Sleeman, C. J. Schofield, *Chem. Commun.* **2005**, *34*, 4251–4263.

[22] R. Li, A. Stapon, J. T. Blanchfield, C. A. Townsend, *J. Am. Chem. Soc.* **2000**, *122 (38)*, 9296–9297.

[23] R. M. Phelan, C. A. Townsend, *J. Am. Chem. Soc.* **2013**, *135 (20)* 7496–7502.

[24] K. Valegård, A. C. T. van Scheltinga, M. D. Lloyd, T. Hara, S. Ramaswamy, A. Perrakis, A. Thompson, H.-J. Lee, J. E. Baldwin, C. J. Schofield, J. Hadju, I. Andersson, *Nature* **1998**, *394 (6695)*, 805–809.

[25] J. Zhou, W. L. Kelly, B. O. Bachman, M. Gunsior, C. A. Townsend, E. I. Solomon, *J. Am. Chem. Soc.* **2001**, *123 (30)*, 7388–7398.

[26] W. Lau, E. S. Sattely, *Science* **2015**, *349 (6253)*, 1224–1228.

[27] H. Li, W. Zhu, Y. Liu, *J. Chem. Inf. Model.* **2019**, *59 (12)*, 5086–5098.

[28] W. Yan, H. Song, F. Song, Y. Guo, C.-H. Wu, A. Sae Her, Y. Pu, S. Wang, N. Naowarojna, A. Weitz, M. P. Hendrich, C. E. Costello, L. Zhang, P. Liu, Y. Jessie Zhang, *Nature* **2015**, *527 (7579)*, 539–543.

[29] Y. Matsuda, T. Bai, C. B. W. Phippen, C. S. Nødvig, I. Kjærbølling, T. C. Vesth, M. Andersen, U. H. Mortensen, C. H. Gotfredsen, I. Abe, T. O. Larsen, *Nat. Commun.* **2018**, *9 (1)*, 2587.

[30] C. Q. Herr, R. P. Hausinger, *Trends Biochem. Sci.* **2018**, *43 (7)*, 517–532.

[31] V. Purpero, G. R. Moran, *J. Biol. Inorg. Chem.* **2007**, *12 (5)*, 587–601.

[32] L.-F. Wu, S. Meng, G.-L. Tang, *Biochim. Biophys. Acta Proteins Proteomics* **2016**, *1864 (5)*, 453–470.

[33] C. A. Townsend, *Curr. Opin. Chem. Biol.* **2002**, *6 (5)*, 583–589.

[34] K.-B. Cho, H. Hirao, S. Shaik, W. Nam, *Chem. Soc. Rev.* **2016**, *45 (5)*, 1197–1210.

[35] S. Martinez, R. P. Hausinger, *J. Biol. Chem.* **2015**, *290 (34)*, 20702–20711.

[36] J. C. Price, E. W. Barr, T. E. Glass, C. Krebs, J. M. Bollinger, *J. Am. Chem. Soc.* **2003**, *125 (43)* 13008–13009.

[37] J. C. Price, E. W. Barr, L. M. Hoffart, C. Krebs, J. M. Bollinger, *Biochemistry* **2015**, *44 (22)*, 8138–8147.

[38] L. M. Hoffart, E. W. Barr, R. B. Guyer, J. M. Bollinger, C. Krebs, *Proc. Nat. Acad. Sci.* **2006**, *103 (40)*, 14738–14743.

[39] S. S. Chaturvedi, R. Ramanan, N. Lehnert, C. J. Schofield, T. G. Karabencheva-Christova, C. Z. Christov, *ACS Catal.* **2020**, *10 (2)*, 1195–1209.

[40] J. A. Hangasky, C. Y. Taabazuing, M. A. Valliere, M. J. Knapp, *Metallomics* **2013**, *5 (4)*, 287.

[41] T. K. Paine, L. Que Jr., *Structure and Bonding*, Springer-Verlag, Berlin, **2014**.

[42] L. Yang, V. J. Colandrea, J. J. Hale, *Expert Opin. Ther. Pat.* **2010**, *20*, 1219–1245.

[43] D. M. Gilkes, P. Chaturvedi, S. Bajpai, C. C. Wong, H. Wei, S. Pitcairn, M. E. Hubbi, D. Wirtz, G. L. Semenza, *Cancer Res.* **2013**, *73*, 3285–3296.

[44] C. H. Hocart, B. Halpern, L. A. Hick, C. O. Wong, J. W. Hammond, B. Wilcken, *J. Chromatogr. Biomed. Appl.* **1983**, *275*, 237–243.

[45] K. Tomoeda, H. Awata, T. Matsuura, I. Matsuda, E. Ploechl, T. Milovac, A. Boneh, C. R. Scott, D. M. Danks, F. Endo, *Mol. Genet. Metab.* **2000**, *71*, 506–510.

[46] A. S. Wierzbicki, M. D. Lloyd, C. J. Schofield, M. D. Feher, F. B. Gibberd, *J. Neurochem.* **2002**, *80*, 727–735.

[47] W. G. Cole, O. Mäkitie, *Textbook of Pediatric Rheumatology*, Saunders, **2016**.

[48] L. Risteli, J. Risteli, A. Ihme, T. Krieg, P. K. Müller, *Biochem. Biophys. Res. Commun.* **1980**, *96*, 1778–1784.

[49] K. I. Kivirikko, *Ann. Med.* **1993**, *25*, 113–126.

[50] C.-K. Liu, C.-A. Hsu, M. T. Abbott, *Arch. Biochem. Biophys.* **1973**, *159*, 180–187.

[51] M. T. Abbott, *Methods Enzymol.* **1967**, *12*, 47–50.

[52] E. Pokidysheva, S. Boudko, J. Vranka, K. Zientek, K. Maddox, M. Moser, R. Fässler, J. Ware, H. P. Bächinger, *Proc. Nat. Acad. Sci.* **2014**, *111*, 161–166.

[53] F. H. Vaillancourt, J. Yin, C. T. Walsh, *Proc. Nat. Acad. Sci.* **2005**, *102*, 10111–10116.

[54] N. R. Rose, M. A. McDonough, O. N. F. King, A. Kawamura, C. J. Schofield, *Chem. Soc. Rev.* **2011**, *40*, 4364.

[55] J. D. Vasta, R. T. Raines, *J. Med. Chem.* **2018**, *61*, 10403–10411.

[56] J. T. Bush, R. K. Leśniak, T.-L. Yeh, R. Belle, H. Kramer, A. Tumber, R. Chowdhury, E. Flashman, J. Mecinović, C. J. Schofield, *Chem. Commun.* **2019**, *55*, 1020–1023.

[57] A. M. Rydzik, R. Chowdhury, G. T. Kochan, S. T. Williams, M. A. McDonough, A. Kawamura, C. J. Schofield, *Chem. Sci.* **2014**, *5*, 1765–1771.

[58] R. J. Hopkinson, A. Tumber, C. Yapp, R. Chowdhury, W. Aik, K. H. Che, X. S. Li, J. B. L. Kristensen, O. N. F. King, M. C. Chan, K. K. Yeoh, H. Choi, L. J. Walport, C. C. Thinnes, J. T. Bush, C. Lejeune, A. M. Rydzik, N. R. Rose, E. A. Bagg, M. A. McDonough, T. J. Krojer, W. W. Yue, S. S. Ng, L. Olsen, P. E. Brennan, U. Oppermann, S. Müller, R. J. Klose, P. J. Ratcliffe, C. J. Schofield, A. Kawamura, *Chem. Sci.* **2013**, *4*, 3110.

[59] P. H. Maxwell, K.-U. Eckardt, *Nat. Rev. Nephrol.* **2016**, *12*, 157–168.

[60] C. Tollnick, G. Siedel, M. Beyer, K. Schügerl, *New Trends and Developments in Biochemical Engineering*, Springer, Berlin, 2004; G. Conti, L. Pollegioni, E. Rosini, *Catal. Sci. Technol.* **2015**, *5*, 1854–1863.

[61] X. Zhang, E. King-Smith, L.-B. Dong, L.-C. Yang, J. D. Rudolf, B. Shen, H. Renata, *Science* **2020**, *369*, 799–806; H. Renata, *Synlett* **2021**, *32 (08)*, 775–784.

[62] E. G. Pavel, J. Zhou, R. W. Busby, M. Gunsior, C. A. Townsend, E. A. Solomon, *J. Am. Chem. Soc.* **1998**, *120*, 743–753.

[63] M. L. Neidig, C. D. Brown, K. M. Light, D. G. Fujimori, E. M. Nolan, J. C. Price, E. W. Barr, J. M. Bollinger, C. Krebs, C. T. Walsh, E. I. Solomon, *J. Am. Chem. Soc.* **2007**, *129*, 14224–14231.

[64] M. L. Neidig, C. D. Brown, M. Kavana, O. W. Choroba, J. B. Spencer, G. R. Moran, E. I. Solomon, *Inorg. Biochem.* **2006**, *100*, 2108–2116.

[65] J. M. Elkins, M. J. Ryle, I. J. Clifton, J. C. Dunning Hotopp, J. S. Lloyd, N. I. Burzlaff, J. E. Baldwin, R. P. Hausinger, P. L. Roach, *Biochemistry* **2002**, *41*, 5185–5182.

Chemistry–A European Journal

Research Article
doi.org/10.1002/chem.202302710

Chemistry Europe
European Chemical
Societies Publishing

[66] A. R. Diebold, C. D. Brown-Marshall, M. L. Neidig, J. M. Brownlee, G. R. Moran, E. I. Solomon, *J. Am. Chem. Soc.* **2011**, *133*, 18148–18160.

[67] E. I. Solomon, K. M. Light, L. V. Liu, M. Srnec, S. D. Wong, *Acc. Chem. Res.* **2013**, *46*, 2725–2739.

[68] M. Srnec, S. D. Wong, J. England, L. Que Jr., E. I. Solomon, *Proc. Nat. Acad. Sci.* **2012**, *109*, 14326–14331.

[69] M. J. Drummond, C. L. Ford, D. L. Gray, C. V. Popescu, A. R. Fout, *J. Am. Chem. Soc.* **2019**, *141*, 6639–6650.

[70] J. R. O'Brien, D. J. Schuller, V. S. Yang, B. D. Dillard, W. N. Lanzilotta, *Biochemistry* **2003**, *42*, 5547–5554.

[71] Y.-M. Chiou, L. Que Jr., *J. Am. Chem. Soc.* **1992**, *114*, 7567–7568.

[72] Y.-M. Chiou, L. Que Jr., *J. Am. Chem. Soc.* **1995**, *117*, 3999–4013.

[73] T. K. Paine, J. England, L. Que Jr., *Chem. Eur. J.* **2007**, *13*, 6073–6081.

[74] E. H. Ha, R. Y. N. Ho, J. F. Krisiel, J. S. Valentine, *Inorg. Chem.* **1995**, *34*, 2265–2266.

[75] S. Hikichi, T. Ogihara, K. Fujisawa, N. Kitajima, M. Akita, Y. Moro-oka, *Inorg. Chem.* **1997**, *36*, 4539–4547.

[76] E. L. Hegg, R. Y. N. Ho, L. Que Jr., *J. Am. Chem. Soc.* **1999**, *121*, 1972–1973.

[77] A. Mukherjee, M. Martinho, E. L. Bominaar, E. Münck, L. Que Jr., *Angew. Chem. Int. Ed.* **2009**, *48*, 1780–1783.

[78] D. Sheet, T. K. Paine, *Chem. Sci.* **2016**, *7*, 5322–5331.

[79] A. Mukherjee, M. A. Cranswick, M. Chakrabarti, T. K. Paine, K. Fujisawa, E. Münck, L. Que Jr., *Inorg. Chem.* **2010**, *49*, 3618–3628.

[80] B. N. Sánchez-Eguía, J. Serrano-Plana, A. Company, M. Costas, *Chem. Commun.* **2020**, *56*, 14369–14372.

[81] E. L. Hegg, L. Que Jr., *Eur. J. Biochem.* **1997**, *250*, 625–629.

[82] A. R. Diebold, M. L. Neidig, G. R. Moran, G. D. Straganz, E. I. Solomon, *Biochemistry* **2010**, *49*, 6945–6952.

[83] A. R. Diebold, G. D. Straganz, E. I. Solomon, *J. Am. Chem. Soc.* **2011**, *133*, 15979–15991.

[84] E. C. Monkcom, D. de Bruin, A. J. de Vries, M. Lutz, S. Ye, R. J. M. Klein Gebbink, *Chem. Eur. J.* **2021**, *27*, 5191–5204.

[85] E. Folkertsma, E. F. de Waard, G. Korpershoek, A. J. van Schaik, N. Solozabal Mirón, M. Borrmann, D. Nijsse, M. A. H. Moelands, M. Lutz, M. Otte, M.-E. Moret, R. J. M. Klein Gebbink, *Eur. J. Inorg. Chem.* **2016**, *2016*, 1319–1332.

[86] P. D. Oldenburg, C.-Y. Ke, A. A. Tipton, A. A. Shteinman, L. Que Jr., *Angew. Chem. Int. Ed.* **2006**, *45*, 7975–7978.

[87] S. C. Bete, M. Otte, *Angew. Chem. Int. Ed.* **2021**, *60*, 18582–18586.

[88] E. C. Monkcom, P. Ghosh, E. Folkertsma, H. A. Negenman, M. Lutz, R. J. M. Klein Gebbink, *Chim. Int. J. Chem.* **2020**, *74*, 450–466.

[89] E. C. Monkcom, H. A. Negenman, E. Masferrer-Rius, M. Lutz, S. Ye, E. Bill, R. J. M. Klein Gebbink, *Eur. J. Inorg. Chem.* **2022**, *9*, e202101046.

[90] Y.-M. Chiou, L. Que Jr., *Angew. Chem. Int. Ed.* **1994**, *33*, 1886–1888.

[91] R. Müller, R. Hübner, N. Burzlaff, *Eur. J. Inorg. Chem.* **2004**, 2151–2159.

[92] A. W. Addison, T. N. Rao, J. Reedijk, J. van Rijn, G. C. Verschoor, *J. Chem. Soc. Dalton Trans.* **1984**, 1349–1356.

[93] P. Gütlich, E. Bill, A. Trautwein in *Mössbauer Spectroscopy and Transition Metal Chemistry: Fundamentals and Applications*, Springer, **2011**.

[94] T. C. Berto, M. B. Hoffman, Y. Murata, K. B. Landenberger, E. Ercan Alp, J. Zhao, N. Lenhert, *J. Am. Chem. Soc.* **2011**, *133*, 16714–16717.

[95] S. Yan, L. Que Jr., L. F. Taylor, O. P. Anderson, *J. Am. Chem. Soc.* **1988**, *110*, 5222–5224.

[96] W. H. Armstrong, S. J. Lippard, *J. Am. Chem. Soc.* **1984**, *106*, 4632–4633.

[97] F. J. Wu, D. M. Kurtz, K. S. Hagen, P. D. Nyman, P. G. Debrunner, V. A. Vankai, *Inorg. Chem.* **1990**, *29*, 5174–5183.

[98] S. Yan, D. D. Cox, L. L. Pearce, C. Juarez-Garcia, L. Que Jr., J. H. Zhang, C. J. O'Connor, *Inorg. Chem.* **1989**, *28*, 2507–2509.

[99] S. Yan, X. Pan, L. F. Taylor, J. H. Zhang, C. J. O'Connor, D. Britton, O. P. Anderson, L. Que Jr., *Inorg. Chim. Acta.* **1996**, *243*, 1–8.

[100] T. C. Harrop, Z. J. Tonzetich, E. Reisner, S. J. Lippard, *J. Am. Chem. Soc.* **2008**, *130*, 15602–15610.

[101] M. Jana, C. J. White, N. Pal, S. Demeshko, C. Cordes, F. Meyer, N. Lenhert, A. Majumdar, *J. Am. Chem. Soc.* **2020**, *142*, 6600–6616.

[102] N. Pal, C. J. White, S. Demeshko, F. Meyer, N. Lehnert, A. Majumdar, *Inorg. Chem.* **2021**, *60 (21)*, 15890–15900.

[103] Y.-M. Chiou, L. Que Jr., *Inorg. Chem.* **1995**, *34*, 3270–3278.

[104] *Metal Nitrosyls*, Oxford University Press, New York, **1992**.

[105] J. H. Enemark, R. D. Feltham, *Coord. Chem. Rev.* **1974**, *13*, 339–406.

[106] Y. Zhang, M. A. Pavlosky, C. A. Brown, T. E. Westre, B. Hedman, K. O. Hodgson, E. I. Solomon, *J. Am. Chem. Soc.* **1992**, *114*, 9189–9191.

[107] C. A. Brown, M. A. Pavlosky, T. E. Westre, Y. Zhang, B. Hedman, K. O. Hodgson, E. I. Solomon, *J. Am. Chem. Soc.* **1995**, *117*, 715–732.

[108] S. Ye, J. C. Price, E. W. Barr, M. T. Green, J. M. Bollinger Jr., C. Krebs, F. Neese, *J. Am. Chem. Soc.* **2010**, *132 (13)*, 4739–4751.

[109] D. M. Ekanayake, A. A. Fischer, M. E. Elwood, A. M. Guzek, S. V. Lindeman, C. V. Popescu, A. T. Fiedler, *Dalton Trans.* **2020**, *49*, 17745–17757.

[110] J. McCracken, P. J. Cappillino, J. S. McNally, M. D. Krzyaniak, M. Howart, P. C. Tarves, J. P. Caradonna, *Inorg. Chem.* **2015**, *54*, 6486–6497.